

Complications of using thin film geometries for nanocrystalline thermal stability investigations

Xuyang Zhou¹, Tyler Kaub¹, Florian Vogel^{1,2}, Gregory B. Thompson^{1,a)} 

¹Department of Metallurgical & Materials Engineering, The University of Alabama, Tuscaloosa, AL 35487, USA

²Institute of Advanced Wear & Corrosion Resistant and Functional Materials, Jinan University, Guangzhou 510632, China

^{a)}Address all correspondence to this author. e-mail: gthompson@eng.ua.edu

Received: 6 April 2020; accepted: 19 June 2020

We report the sputter deposition of Cu-7V and Cu-27V (at.%) alloy films in an attempt to yield a “clean” alloy to investigate nanocrystalline stability. Films grown in high vacuum chambers can mitigate processing contaminants which convolute the identification of nanocrystalline stability mechanism(s). The initial films were very clean with carbon and oxygen contents ranging between ~0.01 and 0.38 at.%. Annealing at 400 °C/1 h facilitated the clustering of vanadium at high-angle grain boundary triple junctions. At 800 °C/1 h annealing, the Cu-7V film lost its nanocrystalline grain sizes with the vanadium partitioned to the free surface; the Cu-27V retained its nanocrystalline grains with vanadium clusters in the matrix, but surface solute segregation was present. Though the initial alloy and vacuum annealing retained the low contamination levels sought, the high surface area-to-volume ratio of the film, coupled with high segregation tendencies, enabled this system to phase separate in such a manner that the stability mechanisms that were to be studied were lost at high temperatures. This illustrates obstacles in using thin films to address nanocrystalline stability.

INTRODUCTION

The use of solute segregation has been found to be a means to impede elevated temperature grain growth in nanocrystalline alloys [1, 2, 3, 4, 5, 6, 7, 8, 9, 10, 11, 12, 13, 14, 15, 16, 17, 18, 19, 20, 21, 22, 23, 24, 25, 26, 27, 28]. The solutes can either “wet” the boundary and provide a thermodynamic reduction in the grain boundary (GB) energy that drives coarsening and/or cluster to precipitate as a secondary phase and provide a kinetic pinning effect [4, 25, 29]. Examples of nanocrystalline stability based on these mechanisms have been reported in Ni(P) alloys, [30, 31]; Cu(Ta) alloys [32]; and Cr(W) [33] to name a few.

Elucidating the specific details of stabilization mechanisms has been a subject of investigation for many decades [3, 20, 21, 24, 34, 35, 36]. For instance, Cahn, in 1962, described a solute drag effect that originated from a competition between the migration of the GB relative to the diffusivity of a solute into or away from the boundary [34]. In more recent years, the thermodynamics of the solute effect on the boundary energy has been emphasized, where the solute has been proposed to reduce the GB energy to values near zero. This would reduce or even eliminate the driving force for grain growth [3, 12, 20, 21, 24, 35]. These thermodynamic concepts were further

developed by considering both the enthalpy of mixing and segregation of the solute species within the solvent matrix [10,21, 24,26]. This led to maps that could guide predictions of stability, metastability, and instability with respect to nanocrystalline grain sizes with temperature [12]. Though the enthalpy of segregation would clearly be necessary to promote solute partitioning to the boundary, the enthalpy of mixing provides guidance if the solute can cluster together and even precipitate as a secondary, separate phase changing the mechanisms of stabilization [12, 24].

In the above approaches, the general concepts have considered the GBs to be isotropic and that partitioning behavior is independent of boundary type. However, it is well known that GBs are diverse in structure and energy. For example, in the aforementioned Ni(P) system, atom probe tomography (APT) revealed inhomogeneous segregation to various boundary types [30, 31]. More recently, X-ray energy-dispersive spectroscopy (XEDS) by transmission electron microscopy (TEM) in nanocrystalline-stabilized Pt(Au) revealed a variation of Au content as a function of different GBs [37]. Recent work by the authors group has clearly linked differences in solute segregation to different GB types in Fe(Cr) [38]. Thus, the



ability to correlate the solute to the boundary type provides a further level of information on their interdependent role in stabilization and thereby provides a comprehensive map on the partitioning behavior and its effect on stabilization.

Beside solute-boundary specificity, a more pressing concern regarding stability is to properly identify the stabilization mechanism. Kapoor et al. [39] have shown, by APT, the presence of nanoscale carbide and oxide clusters in Cu(Nb) boundaries formed from intrinsic reactions of the solute with contaminants from the ball milling process that made the nanocrystalline alloy. Similarly, in Fe(Mg), upon heating the sample under high vacuum, the oxygen reacted with both matrix and solute species creating oxide phases which convolute the underlying metallic phase stability mechanisms [40]. In work reported by Marvel et al. [41, 42], the formation of nanoscale carbides and other deleterious by-products from the electrodeposition of nanocrystalline Ni(W) convolute the predicted thermodynamic stability as the underlying mechanism. In all of these cases, the formation of other phases with either the solute or the solvent and/or both complicate the ability to ascertain the underlying mechanism(s) responsible for stability generating debate in the literature.

In this paper, we have undertaken an investigation to use sputter deposition to secure a “cleaner” system free from ball milling pick-up or by-products in electrochemical reactions. Sputtering is nominally done under (ultra) high vacuum base conditions with the flow of an ultra-high purity gas to higher pressures as the plasma gas source. These, along with controlled levels of target impurities, regulate the extent of environmental and intrinsic material effects on impurity levels in the final film deposit, with the films themselves being nanocrystalline. Furthermore, through the use of cross-correlative microscopy [43], one can then link the solute partitioning to the specific boundary types [38, 44] in these “cleaner” boundaries.

Our case study will be Cu(V), where vanadium is a transition group VB metal and is in the same family as tantalum and niobium. Of the proposed nanocrystalline alloys, the Cu(Ta) system has been well documented and largely agreed upon to be a nanocrystalline stabilized system [32]. However, tantalum, when compared with niobium, is nearly 25× more in cost providing an economic consideration in scale-up. As a result, Kapoor et al. [39] provided a companion study to determine if Cu(Nb) alloys are also thermally nanocrystalline stable, which was confirmed. However, as noted above, in the Cu(Nb) system at least, nanoscale oxide clusters, and even Fe, were found in the boundaries from pick-up from the ball milling process. These small clusters were noted as potential mechanisms for pinning effects to the boundaries, at least in low-solute concentration regimes. We now extend our study to vanadium. Similar to tantalum and niobium, vanadium

has a high, positive enthalpy of segregation with copper and should, in principle, exhibit similar nanocrystalline stability. Finally, vanadium is highly sensitive to reacting and forming carbides, oxides, and nitrides as well and would be an ideal solute to determine the “cleanness” of the sputter-deposited films.

RESULTS AND DISCUSSION

Table 1 tabulates the average grain size of the different Cu(V) films measured from TEM and precession electron diffraction (PED) data. For the ambient temperature deposition, with increasing solute content, the mean grain size refined. In prior work by the authors on other nanocrystalline systems [38], the addition of a partitioning solute has been shown to segregate to the GBs even at room temperature deposition conditions. This solute partitioning is linked to the extent of segregation enthalpy and facilitates the grain refinement. Clearly, the higher the solute content for this immiscible alloy, the further grain refinement is promoted. Upon annealing each composition at 400 °C/1 h, the average grain size in both alloys increased, with Cu-7V being ~40% and Cu-27V nearly a 100%. Nevertheless, the grain sizes are still well within the nanocrystalline regime at 55 ± 31 nm (Cu-7V) and 27 ± 13 nm (Cu-27V). The most dramatic change in grain size occurs when annealing at 800 °C/1 h for the Cu-7V film, where the grains are >1000 nm, and in the case of the APT tip of this specimen, Fig. 1, a GB was not even captured in the region of interest. The Cu-27V film showed continuous grain coarsening, with a tripling of the mean grain size to 87 ± 44 nm, but the grain growth is considerably less. Thus, it appears that the nanocrystalline stability may be a factor of the solute content, which would be peculiar as in the prior bulk processed Cu(Ta) [32] and Cu(Nb) [39] the solute contents were <10 at.% and reported to be sufficient to prevent large grain growth at these temperatures.

Figure 1 shows the cross-correlative TEM–APT tips for each of the compositions in each of the annealed states. The subset of images within Figs. 1(a)–1(d) are the bright field, PED orientation, GB mapping, XEDS spectral mapping, and corresponding APT reconstructions. The field evaporation characteristics of these clusters shown in the APT reconstructions were recently described by the authors, and the interested readers are referred to that reference [45]. In all four conditions, the presence of V clusters is apparent and has been

TABLE 1: Grain size of Cu-7V and Cu-27V alloy films varying with an annealing temperature as determined by TEM.

Temperature	Cu-7V (nm)	Cu-27V (nm)
Ambient temperature	40 ± 21	14 ± 6
400 °C	55 ± 31	27 ± 13
800 °C	>1000	87 ± 44

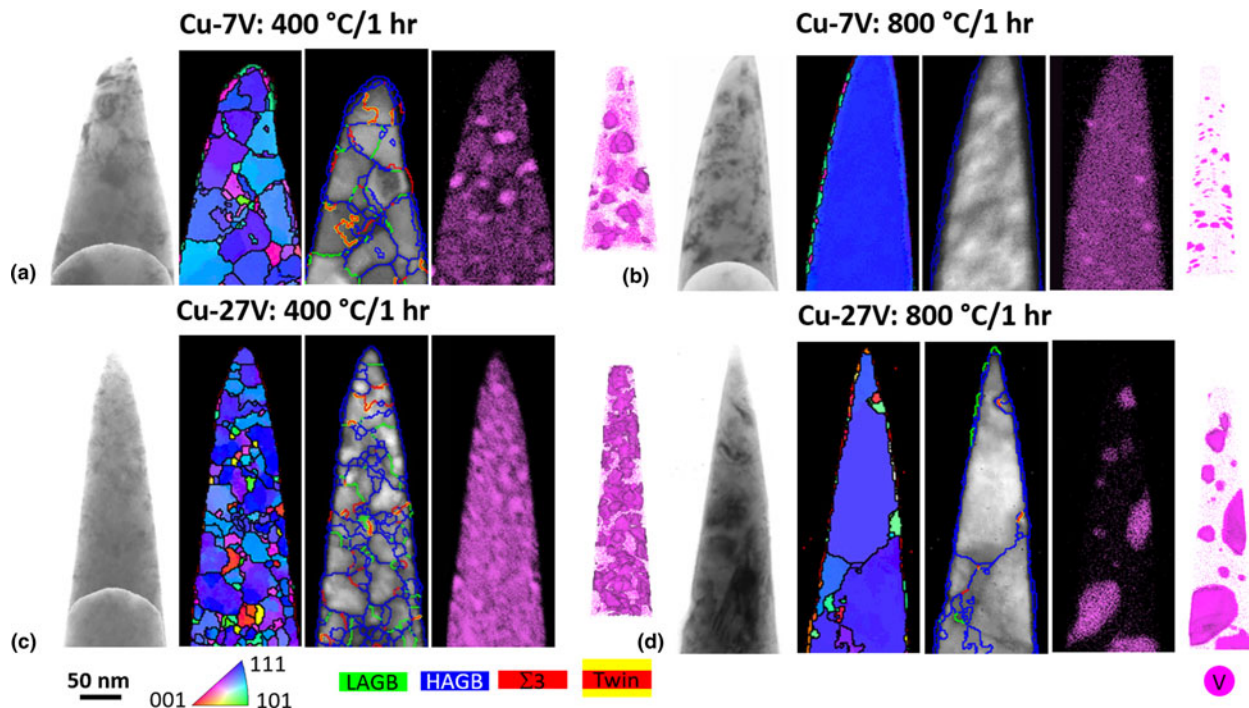


Figure 1: Microstructure and composition mapping of Cu-7V (a) and (b) and Cu-27V (c) and (d) annealed at 400 °C (a) and (c) and 800 °C (b) and (d) for 1 h. Each subfigure shows, from left to right, the TEM bright field image, PED orientation mapping, GB map, EDX composition mapping of V, and APT reconstructed map of V atoms with 50 at.% V isoconcentration surfaces overlaid.

highlighted with the same isoconcentration surface, i.e., 50 at.% V, albeit the size and number density differ between each of the tips. Correlating the GB maps in Fig. 1, we note that the samples are dominated by high-angle GBs, with the clusters located at the triple junctions. Thus, in these samples, a special GB character is likely not a contributing factor in either the solute partitioning and/or stabilization behavior. The formation of clusters at triple junctions would follow conventional physical metallurgy principles where GBs are potent heterogeneous nucleation sites and fast diffusion pathways for solutes to migrate together [46, 47].

The pinning of the grain growth appears to be from these clusters located at the triple junctions. However, there are some subtle differences in behavior. For example, at 400 °C/1 h, the

XEDS map and APT reconstruction for the Cu-7V alloy qualitatively revealed a lower number and slightly larger-sized clusters when compared with the same heat treatment condition as the Cu-27V sample, Fig. 1(c), with quantitative values for these features given in Table 2. The Cu-27V alloy shows a qualitatively higher V content in the grains, evident by the spectral XEDS map. In Table 2, we note that the number density of vanadium clusters in the Cu-7V is about twice that of the Cu-27V alloy, but the ratio of vanadium found in the clusters versus all ions captured in the dataset remains the same, i.e., 16%. This indicates that both samples underwent a similar segregation process, but with a higher nucleation density in the Cu-27V alloy because of its higher solute content. The spacing between clusters was measured via a self-developed algorithm.

TABLE 2: Bulk composition, cluster core composition, number of V clusters, their number density, volume fraction, cluster size, cluster spacing, and the ratio of V ions found within V clusters to all V ions measured in the APT tips shown in Fig. 1.

Parameters	Cu-7 V @400 °C	Cu-27 V @400 °C	Cu-7 V @800 °C	Cu-27 V @800 °C
Vanadium bulk composition	7.0%	27.1%	0.1%	4.8%
Cluster core composition	100 ± 11% V	100 ± 8% V	100 ± 11% V	54 ± 5% V, 46 ± 3% O
Clusters number	44	71	8	10
Number density ($\times 10^{24} \text{ m}^{-3}$)	0.06	0.13	0.01	0.01
Volume fraction	5%	20%	0.03%	10%
Cluster size (nm)	8.2 ± 5.9	8.4 ± 7.7	3.0 ± 0.8	14.5 ± 13.9
Cluster spacing (nm)	46 ± 32	41 ± 36	58 ± 29	89 ± 56
$V_{\text{in clusters}}/V_{\text{all ions}}$	0.16	0.16	0.02	0.71

The V clusters were found by using the LCM. The annealing time is 1 h for all films.

The reader is referred in the Supplementary Material for further details on this method. It was found that the spacing between clusters in the Cu-7V sample is 46 ± 32 nm, with the Cu-27V being 41 ± 36 nm. It is worth to mention that this spacing is similar to the average grain size of the samples, 55 ± 31 nm for Cu-7V and 27 ± 13 nm for Cu-27V, indicating that the nucleation of V clusters likely occurs along around the grains evident by the cluster locations in Fig. 1. For the Cu-7V sample, the maximum separation method (MSM) is provided for comparison. Note that the MSM method is able to provide analysis for 7V but not for 27V, as it is designed for low-solute content where the frequency of detecting another atom of the same type is low for general randomness, which enables a higher confidence for cluster detection. Using MSM provides additional guidance on the isoconcentration surface selection value for the local concentration method (LCM) analysis. Details on the MSM selection criteria are also provided in the Supplementary Material of this paper. The compositional quantification of the clusters found in the atom probe tips was obtained from 1D profiles shown in the Supplementary Material. In either Cu-7V or Cu-27V, the 400 °C annealed solute concentration at the core of the cluster is close to 100%, Table 2, indicative of a nucleation and growth event than spinodal decomposition of the film.

Using the APT measurements, the vanadium volume fraction and cluster size for each annealed alloy film enabled an estimate of the grain size stabilized by a Zener grain pinning mechanism using the expression:

$$D = \frac{0.4d}{f}, \quad (1)$$

where D is the average grain diameter and f is the volume fraction of precipitates with the average diameter d [48]. The predicted stable grain sizes for the Cu-7V and Cu-27V films are 66 and 17 nm, respectively. The Zener pinning estimation gives a reasonable prediction when comparing with the experimental determined average grain size of ~ 55 nm for Cu-7V and ~ 27 nm for Cu-27V. The stabilization appears dominated by Zener pinning

Upon annealing at 800 °C/1 h, the partitioning of the V evolved. In Fig. 1(b), we note a low number of observable clusters for the Cu-7V, with Table 2 revealing a drop of two orders of magnitude in the volume fraction of such clusters. The clusters that are present are qualitatively smaller when comparing the XEDS maps between Figs. 1(a) and 1(b). Furthermore, Table 2 reveals that the V content in the Cu-7V film, which was 7 at.% V at 400 °C, is now 0.1 at.% V at 800 °C. Similarly, the Cu-27V film went from 27.1 at.% V at 400 °C to 4.8 at.% V at 800 °C. Clearly, the region of interest captured by the APT tips shows a significant loss of solute between the heat treatments, and as a result, a loss in grain stability. For the

Cu-27V sample, at 800 °C, the vanadium clusters/precipitates coarsened at the triple junctions of the high-angle GBs and are still effectively at pinning the grains to some extent, Fig. 1(d). The vanadium that was observed in the Cu-7V film was observed to be small clusters nucleated within the grain itself, Fig. 1(b)'s APT and XEDS images. With such a low amount of vanadium clusters remaining the film, the Zener prediction from Eq. (1) gives an equilibrium grain size of 1600 nm. Thus, without a proper inhibitor (i.e., clusters), the grain size grows rapidly and nanocrystalline stability is lost. Unlike these Cu-7V 800 °C/1 h clusters, which were nearly 100% V in their core, the Cu-27V 800 °C/1 h clusters revealed similar amounts of oxygen as vanadium at their cluster core (Table 2). This is contributed to the latter clusters being more prevalent on the boundaries than encased in the matrix; upon annealing at the higher temperature, they became more susceptible to oxidation at these boundary locations. The calculated Zener pinning grain size from these clusters is approximately 58 nm, which is slightly lower than the experimentally observed grain size of 87 nm. Clearly, the coupled oxidation and thermal stability behavior of the clusters play a complex role in controlling the equilibrium grain size [49].

The obvious question now arises—where has the V gone with higher annealing treatment? Figures 2(a) and 2(b) are the TEM cross-sections with both a PED map and a XEDS spectral map for these two 800 °C annealed films. The foils reveal that the V has strongly partitioned, and wetted, the surface of the Cu film forming a bilayer structure. This is much like how Cr surface protects stainless steel alloys [50] and surface segregation in aluminum alloys [51]. Thus, the stability of the copper grains is lost because the solute is no longer clustering and pinning the grains but has migrated to the surface.

An APT tip, shown in the projected region of the XEDS map for both samples, was prepared and the reconstruction is shown in Fig. 2(c). By creating a 50 at.% V isoconcentration surface, a proximity histogram (proxigram) of the chemical distribution between the two layers is shown in Fig. 2(d), with the surface and film regions labeled in the plot. As expected, the surface layer is V-rich, with a small amount of copper. Upon inspection of the bulk-phase diagram, vanadium can accommodate a small fraction of copper in solution, whereas copper has no solubility of vanadium which explains the rapid purging of V from the copper matrix upon annealing. In the proxigram, we note that the elemental oxygen content in the film was ~ 0.01 at.% and only raised to ~ 0.5 at.% near the surface for the Cu-7V alloy, Fig. 2(di). We also detect silicon in the film and on the surface albeit at a slightly lower concentration but whose profile mimics that of oxygen. Initially, it was thought that the thermally grown silica surface would provide a sufficient diffusion barrier between the film and the silicon substrate, which it was, but a fraction of the silica appears to

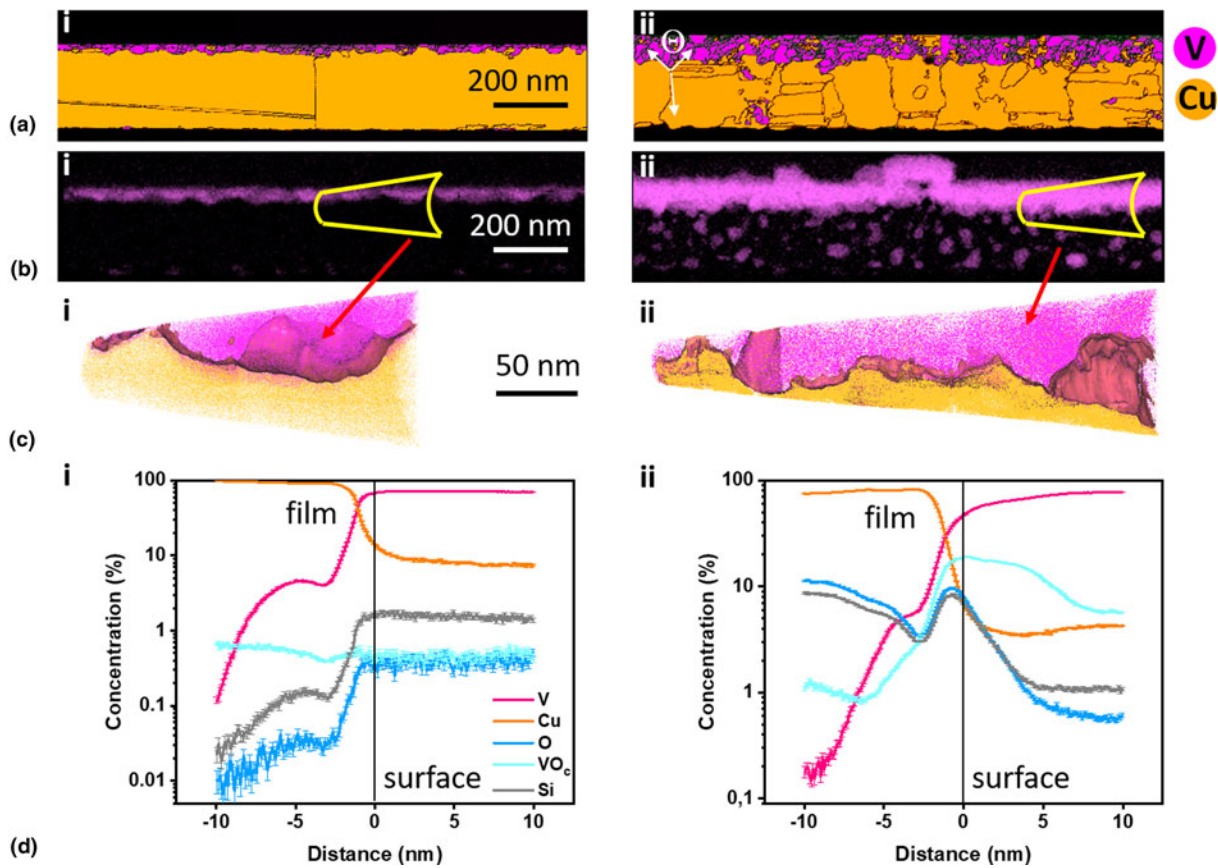


Figure 2: (a) Phase maps generated from PED reconstructions, (b) V concentration maps from EDX, (c) APT reconstruction maps with 50 at.% V isoconcentration surfaces embedded, and (d) the corresponding proxigrams for (i) Cu-7V film and (ii) Cu-27V films annealed @800 °C for 1 h.

diffuse through the film and to its surface. We also note the detection of vanadium oxide complexes during the field evaporation of these samples with the composition denoted as $V-O_c$ in the proxigram. The mass spectrums of these samples are provided in the Supplementary Material. For the Cu-7V film, these oxide complexes were ~1 at.% and uniform within the film and the partitioned V surface. The presence of vanadium oxide is not necessarily surprising considering its affinity for oxygen noted in the Introduction. A very limited overall oxygen contamination was observed in the 400 °C annealed samples, <0.1 at.% for Cu-7V and ~0.38 at.% for the Cu-27V, suggesting that it was picked up during the higher vacuum anneal and not necessarily intrinsic to the film during deposition.

In Fig. 3, the atom maps of oxygen for the Cu-7V and Cu-27 samples are shown. No preference of oxygen partitioning was visualized in either the datasets. The overall compositions for the 400 °C and 800 °C Cu-V-annealed samples are tabulated in Table 3. This leads to addressing the question if sputtering was able to yield a “cleaner” sample. Potential contaminant species, such as carbon and nitrogen, were found to be <0.02 at.% (except for the Cu-27V 800 °C annealed sample, whose the carbon content is 0.53 at.%), demonstrating that indeed “cleaner” nanocrystalline alloys can be fabricated by

sputtering when compared with the prior discussed means such as ball milling and electrodeposition. The mass spectrums of these particular APT datasets are also located in the Supplementary Material. Other than the species listed in Table 3, no other atom types (other than hydrogen) were detected and/or were at levels far less than those reported earlier. The observation of hydrogen and metal hydride atom types is a known artifact related to focused ion beam (FIB)

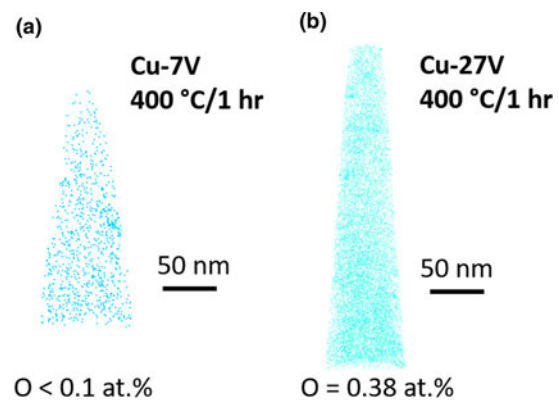


Figure 3: APT reconstructed maps of O atoms for (a) Cu-7V 400 °C/1 h and (b) Cu-27V 400 °C/1 h.

TABLE 3: The compositional quantification of the tips shown in Fig. 1.

Composition (at.%)	Cu-7V @400 °C	Cu-27V @400 °C	Cu-7V @800 °C	Cu-27V @800 °C
Cu	92.78	72.38	99.77	89.50
V	7.04	27.07	0.09	4.75
O	0.08	0.38	0.08	5.14
C	0.02	0.00	0.01	0.53
Si	0.08	0.17	0.05	0.08

sample preparation and laser-assist field evaporation [52] with the details discussed in a prior paper by the authors [45]. We are not confident in being able to distinguish the intrinsic hydrogen contamination from artificial hydrogen detected; therefore, it is not developed further for the context of this work.

Though the thin film growth conditions were sufficient to reduce the amount of contaminants, the access to the free surface provides a clear challenge of using thin films, at least of this alloy, for these types of stability studies. Even the choice of the contact substrate to the film requires further scrutiny evident by the silica compositional profile in Fig. 2. The environmental effects from annealing (oxidation), even in a very clean testing condition, appears to be present as a function of the annealing temperature. Each of these issues should be considered and addressed when other nanocrystalline alloys are studied by this fabrication method. Nevertheless, the phase separation behavior in Cu(V) does provide an opportunity to better understand partitioning effects in thin film microstructures.

The Cu-27V alloy shows very similar vanadium surface partitioning to the Cu-7V film. By virtue of having higher solute content, the vanadium surface layer is thicker than that of the Cu-7V alloy, i.e., compare Figs. 2(a) and 2(b). The APT histogram also reveals similar trends of the species in the bulk of the film and in the surface layer, which include both the oxygen and silicon tracking with each other. In this case, we noted nearly a 10 at.% concentration level for these species in the film. In addition, a notable “bump” at the bilayer interface for these two species is observed in Fig. 2(dii). Small particles of silica in this region were detected from the XEDS map (shown in the Supplementary Material) which microstructurally confirmed the observed behavior captured in the program. As before, vanadium oxide complexes were present and increased in concentration at the surface when compared with the bulk film, indicating that the high temperature annealing environment is the oxygen source and not intrinsic oxygen from the film deposition. Though oxidation is noted, the relatively low amount of oxygen, and the presence of elemental vanadium still on the surface, does indicate that near ultra-high vacuum annealing can (at least) mitigate rampant oxidation contamination for nanocrystalline studies.

Noting that the solute strongly partitions to the GBs and then migrates to the free surface, we have estimated the diffusion distance using an activation energy, Q , of 215 kJ/mol [53], which is on par for GB diffusion for the two temperatures over an anneal time of 60 min. Using the simple approximation that the diffusion distance scales as \sqrt{Dt} , where D is the diffusivity and t is time, the diffusion distance was either 5 or 5500 nm at 400 °C and 800 °C, respectively. Since there was minimal to no solute segregation to the film’s free surface at 400 °C, but clustering in the GBs, the shorter estimated diffusion path length contributed to this first stage of chemical partitioning of the solute from the matrix. Upon annealing to the higher temperature, the estimated diffusion length is now larger than the film thickness (1000 nm). Thus, at this higher temperature condition, it would be sufficient for the solute to easily reach and now enrich the free surface. The presence of some clusters in the Cu-27V/800 °C anneal is contributed to its much higher vanadium content and the potential difficulty for the solutes to “break away” from the larger cluster and diffuse to the free surface. Furthermore, the preference of the solute on the surface is a result of its ability to lower the overall system’s energy. Using a simple interfacial energy balance, the grooving of the boundaries at the free surface can be used to estimate the relative ratio of the surface energies. Figure 2(aii) shows the energy balance configuration (white arrows) for such a groove with the contact angle, Θ . For this condition, the γ_{gb}/γ_{fs} , where γ is the interfacial energy for either the GB or free surface (fs), is 1.4.

To better understand the tendency for segregation to the free surface, we employed a hybrid Monte Carlo (MC) and molecular dynamic (MD) simulation [54]. For the Cu-7V sample, a single grain structure was constructed, which matches the experiments in that once the solute left the film, the underlying Cu grains become quite large. In Fig. 4(a), a $20 \times 20 \times 20 \text{ nm}^3$ structure is shown with the X and Y being periodic directions and Z being the free surface direction. One end of the Z-free surface was fixed to avoid translation of the simulated unit cell. Figure 4(b) reveals the distribution of the 7 at.% vanadium atoms at 800 °C after 2000 ps with a time step of 0.002 ps. At the elevated temperature, the vanadium atoms partitioned together to form large clusters on the free surface [Fig. 4(b)]. Though we did not experimentally see distinct clusters of vanadium on the free surface, the surface showed irregular vanadium distributions giving confidence that the general aspects of the simulations have captured the physics of our experiment. For the Cu-27V sample, the film at 800 °C still retained a nanoscale grain size. Consequently, our initial simulated structure was polycrystalline within the $20 \times 20 \times 20 \text{ nm}^3$ volume. Upon simulating the 800 °C anneal for 2000 ps, large and numerous clusters are observed. Unlike the single-crystal Cu-7V simulation, where the solute clusters were on the free

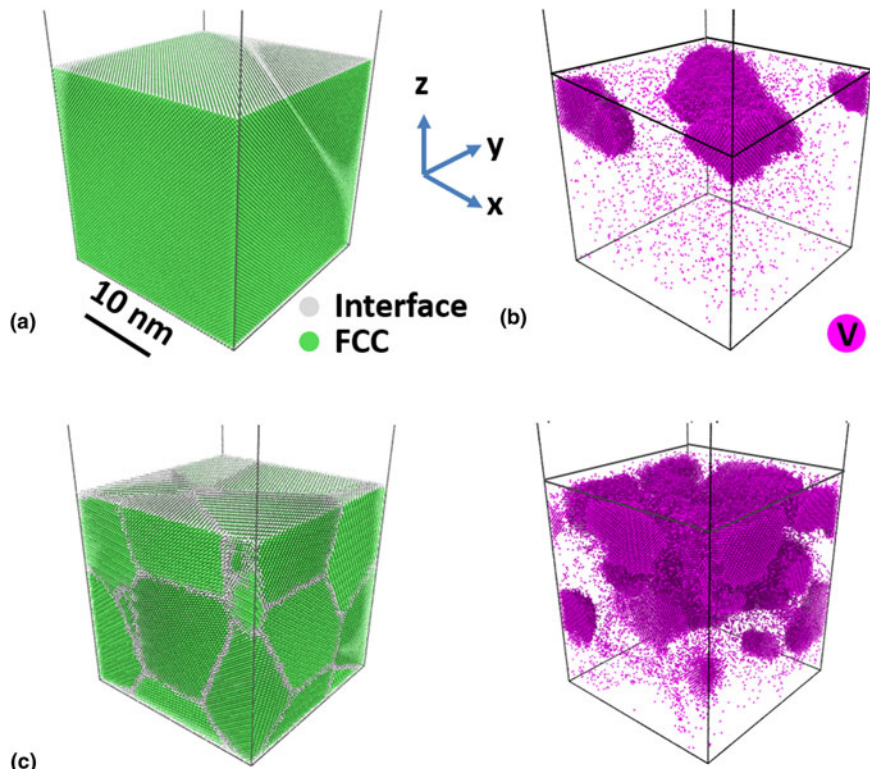


Figure 4: (a) Single grain structure of the Cu-7V sample. (b) The corresponding elemental distribution map of solute V atoms in the single Cu-7V grain after running MC/MD simulation at 800 °C. (c) Polycrystalline structure of the Cu-27V sample. (d) The corresponding elemental distribution map of solute V atoms in the polycrystalline Cu-27V grains after running MC/MD simulation at 800 °C. X and Y are periodic directions, while Z is the free surface.

surface, the polycrystalline simulation for the larger Cu-27V alloy reveals clusters at or near the surface as well as within the GBs, which again matches our experiment [Fig. 2(d)]. The presence of the boundaries serves as defect surface from which the vanadium appears to segregate too and can be retained to some respect in the matrix to mitigate the copper grain growth. Though the decreasing content of vanadium between the two anneal temperatures does suggest, given time, the vanadium will eventually migrate to the surface.

CONCLUSION

In this study, we addressed three major points related to nanocrystalline stability. The first was to determine if solutes of the same family in the periodic table, which also have similar thermodynamic properties with respect to an equivalent matrix species, would provide nanocrystalline stability. Prior reports have shown that bulk Cu(Ta) and Cu(Nb) are stabilized alloys, evident by small solute clusters/precipitates that pin GBs. Similar stability was found in the test case Cu(V), up to a temperature of 400 °C. The formation of clusters/precipitates was noted with a concentration close to pure vanadium. Those newly formed vanadium clusters provided a kinetic pinning effect to copper's grain growth. Through cross-correlative microscopy, these clusters were observed in the triple junctions of high-angle GBs. The ability to ascertain the boundary character information provides forward experimental information

into the boundary types that contribute to stability, the second aim of the paper.

Upon annealing the Cu(V) films to 800 °C for 1 h, the low-solute alloy, Cu-7V, exhibited large grain coarsening (>1000 nm) and the loss of nanocrystalline stability. APT analysis confirmed that <1 at.% V was still in the matrix and that the solute itself was largely distributed as very fine clusters within the grain (and not at the boundaries). Consequently, the solute, at this condition, provided no stabilization effect. The vanadium had migrated to the surface of the film creating a bilayer film. Thus, the thin film geometry, with a relative thin thickness (~200 nm) coupled with the solute's high segregation tendency, enabled the solute effect for stabilization to be removed upon annealing.

When the solute content is sufficiently high, stabilization at higher temperatures is still possible by some retention of the solute clusters in the film. Nevertheless, the solute still partitions to the surface. This behavior was observed in the Cu-27V film. Vanadium clusters/precipitates were located in the triple junctions and upon annealing at 800 °C, and some fraction of these clusters was still retained yielding a matrix with a vanadium content of ~5 at.%. At this higher temperature, these retained clusters oxidized and coarsened.

APT analysis across the interface of the vanadium surface layer in each film revealed the migration of the silica species from the substrate through the film as well as the preferential oxidation of vanadium, although the concentration was low

and largely located only at the surface once vanadium partitioned to this location. Thus, to the third point of the study, sputter deposition appears to provide a cleaner means of fabricating nanocrystalline alloys when compared with ball milling and electrodeposition, but it too is fraught with its own set of issues for stability investigations. By virtue of the thin film geometry, where access to a free surface is readily available, the high segregation tendency, at least for this particular solute species, appears to be sufficient to drive the solute to the free surface at higher temperatures thereby removing the intended stability effect that is to be studied. With the solute on the surface, it reacted with residual oxygen in a near ultra-high vacuum anneal, and a small amount oxidation was noted. Clearly, once the solute is no longer present in the matrix's GBs, stability is lost and the ability to ascertain intrinsic thermodynamic and/or kinetic contributions to stability of the solute is not possible. Furthermore, the substrate for the film itself may also react or at least decompose and provide migration of its own species through the film. Thus, one may be able to fabricate, by sputtering, a sample that is "freer" from the convoluting contaminant aspects of processing; however, the system itself, by virtue of its larger free surface-to-volume ratio, results in a loss of the alloy mixing needed to study this effect. Consequently, particular systems may be more or less amenable for nanocrystalline stability studies as thin films, with this paper highlighting potential issues that may arise.

METHODOLOGY

Two Cu(V) alloy films were sputter-deposited with targeted compositions of Cu-7 at.% V and Cu-27 at.% V by co-magnetron sputtering from 99.95 at.% pure elemental Cu and V targets in an AJA ATC-1500 stainless steel chamber. Prior to deposition, the base pressure was $<6 \times 10^{-6}$ Pa whereupon ultra-high purity Ar was flowed at 10 standard cubic centimeters per minute into the chamber to a pressure of 0.27 Pa. The films were deposited to an approximate thickness of 200 nm onto 300 μm thick silicon [100] substrates that had a thermally grown 100 nm oxide on the surface to provide a diffusion barrier for any deleterious reactions of the film with the substrate. After deposition, the films were annealed at either 400 or 800 °C in a custom-constructed vacuum chamber for 1 h. The base pressure during annealing was $<1 \times 10^{-4}$ Pa.

The grain size and overall structure of the nanocrystalline Cu(V) alloys were imaged and characterized in a Tecnai F20 (S)TEM operated at 200 keV. The cross-section TEM foils were prepared using a FIB milling procedure similar to references [55] in either a TESCAN LYRA FIB-Field Emission Scanning Electron Microscope (SEM) or an FEI Quanta 3D dual-beam FIB-SEM. To obtain a plan-view image, we attached the lifting wedge to a 90° rotation needle. Another lift-out was

conducted on the rotated wedge for cross-section TEM foil preparation. The grain-to-grain mapping for each cross-section foil was conducted using PED on the Nanomegas ASTAR™ platform with the beam precessed at 0.2° at a scanning step size of 3 nm. Post-scanning, the PED data were analyzed using the TSL OIM Analysis 7 software package.

APT quantified the overall film composition and local element distribution for each sample. The required needle-shaped geometry for field evaporation by APT was prepared in the same manner as the previous plan-view TEM foil preparation method using a FIB lift-out technique and annular milling in the dual-beam FIB. The Ga ion implantation in our needles, after the low keV clean-up, was less than 0.1%. We did not include Ga ions in the mass quantification. With the APT tip prepared, the specimen was loaded into a Hummingbird TEM holder and placed into the FEI Tecnai F20 (S)TEM where PED scans of each tip were performed to reveal the grain structure characteristics prior to atom probe field evaporation. Here, the beam was still precessed at 0.2° but at a scanning step size of 2 nm. While the tip was in the TEM, XEDS was collected to provide a complementary chemical spectral map of the elemental distribution to coincide with the APT reconstruction. With the TEM analysis completed, the tips were field evaporated in a Cameca Instruments Local Electrode Atom Probe (LEAP) 5000 XS operated at a specimen set point temperature of 50 K and a laser pulse energy of 100 pJ at a pulse repetition rate of 500 kHz for a 0.5% atoms per pulse detection rate. The APT data were reconstructed using the IVAS 3.8.2 software platform. Further details on the PED and APT cross-correlative study process can be found in Refs [38, 44, 56].

For the APT cluster analysis, the LCM was used to help visualize and quantify the clusters [57, 58] using a 1 nm voxel, which was found to be sufficient since this is smaller than the feature size of interest while still large enough to avoid significant noise from local compositional fluctuations. The MSM was applied for the quantification of the cluster characteristics with the details given in the Supplementary Material of this paper [59, 60, 61].

The polycrystalline structure was constructed by using the atom eye software package [62] with Ovito [63] as the post-processing and visualization platform. In the unit volume, eight points were randomly assigned to the center of each grain. The volume was then filled by grains of different orientations. This created the polycrystalline structures which were then relaxed using the MD conjugate gradient minimization energy procedure. Using those polycrystalline structures, we have employed a hybrid MD and MC [54] to determine the preferential segregation of V into the Cu boundaries. The simulation code was run using LAMMPS with the embedded atom model Cu-V potential [64]. The V concentration was selected

close to the experimental composition, which was 7 at.% V and 27 at.% W. To obtain this concentration, we adjusted the system's chemical potential until the V content matched the target composition. We performed a variance-constrained semi-grand-canonical ensemble in our simulation to capture the phase separation in the immiscibility gap region. One MC cycle was carried out per 10^2 MD steps with the time step being 2000 ps. Nose–Hoover thermostat maintained system temperature. It is worth to mention that MC simulation was designed to search for the sample's equilibrium state, which is a non-diffusional process and does not provide information on the kinetics of the segregation process [37]. To approach an equilibrium state, the simulations were run for 10^6 steps.

Acknowledgment

The authors gratefully acknowledge NSF-DMR-1709803 for support of this work.

Supplementary material

To view supplementary material for this article, please visit <https://doi.org/10.1557/jmr.2020.174>.

References

1. **A. Detor and C. Schuh:** Grain boundary segregation, chemical ordering and stability of nanocrystalline alloys: Atomistic computer simulations in the Ni–W system. *Acta Mater.* **55**(12), 4221 (2007).
2. **C. Koch, R. Scattergood, K. Darling, and J. Semones:** Stabilization of nanocrystalline grain sizes by solute additions. *J. Mater. Sci.* **43**(23–24), 7264 (2008).
3. **C. Koch, R. Scattergood, M. Saber, and H. Kotan:** High temperature stabilization of nanocrystalline grain size: Thermodynamic versus kinetic strategies. *J. Mater. Res.* **28**(13), 1785 (2013).
4. **E. Nes, N. Ryum, and O. Hunderi:** On the zener drag. *Acta Metall.* **33**(1), 11 (1985).
5. **K.A. Darling, B.K. VanLeeuwen, C.C. Koch, and R.O. Scattergood:** Thermal stability of nanocrystalline Fe–Zr alloys. *Mater. Sci. Eng., A* **527**(15), 3572 (2010).
6. **A. Khalajhedayati and T.J. Rupert:** High-temperature stability and grain boundary complexion formation in a nanocrystalline Cu–Zr alloy. *JOM* **67**(12), 2788 (2015).
7. **F. Liu and R. Kirchheim:** Nano-scale grain growth inhibited by reducing grain boundary energy through solute segregation. *J. Cryst. Growth.* **264**(1–3), 385 (2004).
8. **J. Weissmuller:** Some basic notions on nanostructured solids. *Mater. Sci. Eng., A* **179**, 102 (1994).
9. **Y. Chen, Y. Liu, F. Khatkhatay, C. Sun, H. Wang, and X. Zhang:** Significant enhancement in the thermal stability of nanocrystalline metals via immiscible tri-phases. *Scr. Mater.* **67**(2), 177 (2012).
10. **D. Gupta:** Diffusion, solute segregations and interfacial energies in some material: An overview. *Interface Sci.* **11**(1), 7 (2003).
11. **T. Chookajorn and C.A. Schuh:** Nanoscale segregation behavior and high-temperature stability of nanocrystalline W–20at.% Ti. *Acta Mater.* **73**, 128 (2014).
12. **H.A. Murdoch and C.A. Schuh:** Estimation of grain boundary segregation enthalpy and its role in stable nanocrystalline alloy design. *J. Mater. Res.* **28**(16), 2154 (2013).
13. **K.A. Darling, B.K. VanLeeuwen, J.E. Semones, C.C. Koch, R.O. Scattergood, L.J. Kecskes, and S.N. Mathaudhu:** Stabilized nanocrystalline iron-based alloys: Guiding efforts in alloy selection. *Mater. Sci. Eng., A* **528**(13–14), 4365 (2011).
14. **H. Peng, Y. Chen, and F. Liu:** Effects of alloying on nanoscale grain growth in substitutional binary alloy system: Thermodynamics and kinetics. *Metall. Mater. Trans. A* **46A**(11), 5431 (2015).
15. **A. Detor and C. Schuh:** Tailoring and patterning the grain size of nanocrystalline alloys. *Acta Mater.* **55**(1), 371 (2007).
16. **T. Rupert, W. Cai, and C. Schuh:** Abrasive wear response of nanocrystalline Ni–W alloys across the Hall–Petch breakdown. *Wear* **298**, 120 (2013).
17. **V. Novikov:** Grain growth in nanocrystalline materials. *Mater. Lett.* **159**, 510 (2015).
18. **M. Hillert and B. Sundman:** A treatment of the solute drag on moving grain boundaries and phase interfaces in binary alloys. *Acta Metall.* **24**(8), 731 (1976).
19. **R. Kirchheim:** Grain coarsening inhibited by solute segregation. *Acta Mater.* **50**(2), 413 (2002).
20. **J.R. Trelewicz and C.A. Schuh:** Grain boundary segregation and thermodynamically stable binary nanocrystalline alloys. *Phys. Rev. B* **79**(9), 094112 (2009).
21. **K.A. Darling, M.A. Tschopp, B.K. VanLeeuwen, M.A. Atwater, and Z.K. Liu:** Mitigating grain growth in binary nanocrystalline alloys through solute selection based on thermodynamic stability maps. *Comput. Mater. Sci.* **84**, 255 (2014).
22. **M. Saber, C. Koch, and R. Scattergood:** Thermodynamic grain size stabilization models: An overview. *Mater. Res. Lett.* **3**(2), 65 (2015).
23. **S. Sooraj, V. Muthaiah, P. Kang, C. Koch, and S. Mula:** Microstructural evolution and thermal stability of Fe–Zr metastable alloys developed by mechanical alloying followed by annealing. *Philos. Mag.* **96**(25), 2649 (2016).
24. **T. Chookajorn, H.A. Murdoch, and C.A. Schuh:** Design of stable nanocrystalline alloys. *Science* **337**(6097), 951 (2012).

25. **J. Weissmüller:** Alloy effects in nanostructures. *Nanostruct. Mater.* **3**, 261 (1993).
26. **R. Kirchheim:** Reducing grain boundary, dislocation line and vacancy formation energies by solute segregation. I. Theoretical background. *Acta Mater.* **55**(15), 5129 (2007).
27. **J. Drolet and A. Galibois:** Impurity-drag effect on grain growth. *Acta Metall.* **16**(12), 1387 (1968).
28. **F. Abdeljawad and S.M. Foiles:** Stabilization of nanocrystalline alloys via grain boundary segregation: A diffuse interface model. *Acta Mater.* **101**, 159 (2015).
29. **C.S. Smith:** Introduction to grains, phases, and interfaces: an interpretation of microstructure. *Trans. Metall. Soc. AIME* **175**, 15 (1948).
30. **B. Farber, E. Cadel, A. Menand, G. Schmitz, and R. Kirchheim:** Phosphorus segregation in nanocrystalline Ni-3.6 at.% P alloy investigated with the tomographic atom probe (TAP). *Acta Mater.* **48**(3), 789 (2000).
31. **T. Hentschel, D. Isheim, R. Kirchheim, F. Muller, and H. Kreye:** Nanocrystalline Ni-3.6 at.% P and its transformation sequence studied by atom-probe field-ion microscopy. *Acta Mater.* **48**(4), 933 (2000).
32. **T. Rojhirunsakool, K.A. Darling, M.A. Tschopp, G.P.P. Pun, Y. Mishin, R. Banerjee, and L.J. Kecskes:** Structure and thermal decomposition of a nanocrystalline mechanically alloyed super-saturated Cu-Ta solid solution. *MRS Commun.* **5**(2), 333 (2015).
33. **T. Chookajorn, M. Park, and C.A. Schuh:** Duplex nanocrystalline alloys: Entropic nanostructure stabilization and a case study on W-Cr. *J. Mater. Res.* **30**(2), 151 (2015).
34. **J.W. Cahn:** The impurity-drag effect in grain boundary motion. *Acta Mater.* **10**, 789 (1962).
35. **A. Detor and C. Schuh:** Microstructural evolution during the heat treatment of nanocrystalline alloys. *J. Mater. Res.* **22**(11), 3233 (2007).
36. **H.A. Murdoch and C.A. Schuh:** Stability of binary nanocrystalline alloys against grain growth and phase separation. *Acta Mater.* **61** (6), 2121 (2013).
37. **C. O'Brien, C. Barr, P. Price, K. Hattar, and S. Foiles:** Grain boundary phase transformations in PtAu and relevance to thermal stabilization of bulk nanocrystalline metals. *J. Mater. Sci.* **53**(4), 2911 (2018).
38. **X. Zhou, X.-x. Yu, T. Kaub, R.L. Martens, and G.B. Thompson:** Grain boundary specific segregation in nanocrystalline Fe(Cr). *Sci. Rep.* **6**, 34642 (2016).
39. **M. Kapoor, T. Kaub, K.A. Darling, B.L. Boyce, and G.B. Thompson:** An atom probe study on Nb solute partitioning and nanocrystalline grain stabilization in mechanically alloyed Cu-Nb. *Acta Mater.* **126**, 564 (2017).
40. **B. Clark, K. Hattar, M. Marshall, T. Chookajorn, B. Boyce, and C. Schuh:** Thermal stability comparison of nanocrystalline Fe-based binary alloy pairs. *JOM* **68**(6), 1625 (2016).
41. **C.J. Marvel, P.R. Cantwell, and M.P. Harmer:** The critical influence of carbon on the thermal stability of nanocrystalline Ni-W alloys. *Scr. Mater.* **96**, 45 (2015).
42. **C.J. Marvel, B.C. Hornbuckle, K.A. Darling, and M.P. Harmer:** Intentional and unintentional elemental segregation to grain boundaries in a Ni-rich nanocrystalline alloy. *J. Mater. Sci.* **54**(4), 3496 (2019).
43. **J.B. Seol, C.M. Kwak, J.C. Han, K.H. Baek, and Y.K. Jeong:** Correlative transmission electron microscopy and atom probe tomography on field evaporation mechanism of a bulk LaAlO₃ oxide. *Appl. Surf. Sci.* **479**, 828 (2019).
44. **M. Herbig, D. Raabe, Y.J. Li, P. Choi, S. Zaeferrer, and S. Goto:** Atomic-scale quantification of grain boundary segregation in nanocrystalline material. *Phys. Rev. Lett.* **112**(12), 126103 (2014).
45. **X. Zhou, and G.B. Thompson:** Charge-state field evaporation behavior in Cu(V) nanocrystalline alloys. *Microsc. Microanal.* **25**, 501 (2019).
46. **P. Stender, Z. Balogh, and G. Schmitz:** Triple junction segregation in nanocrystalline multilayers. *Phys. Rev. B.* **83**(12), 121407 (2011).
47. **M.R. Chellali, Z. Balogh, and G. Schmitz:** Nano-analysis of grain boundary and triple junction transport in nanocrystalline Ni/Cu. *Ultramicroscopy* **132**, 164 (2013).
48. **R.D. Doherty:** Grain coarsening – Insights from curvature modeling Cyril Stanley Smith Lecture. *Mater. Sci. Forum* **715–716**, 1 (2012).
49. **P.P. Shetty, M.G. Emigh, and J.A. Krogstad:** Coupled oxidation resistance and thermal stability in sputter deposited nanograind alloys. *J. Mater. Res.* **34**(1), 48 (2019).
50. **X. Zhou and G.B. Thompson:** In situ TEM observations of initial oxidation behavior in Fe-rich Fe-Cr alloys. *Surf. Coat. Technol.* **357**, 332 (2019).
51. **Y.F. Qin and S.Q. Wang:** Ab-initio study of surface segregation in aluminum alloys. *Appl. Surf. Sci.* **399**, 351 (2017).
52. **Y.H. Chang, W.J. Lu, J. Guenole, L.T. Stephenson, A. Szczepaniak, P. Kontis, A.K. Ackerman, F.F. Dear, I. Mouton, X.K. Zhong, S.Y. Zhang, D. Dye, C.H. Liebscher, D. Ponge, S. Korte-Kerzel, D. Raabe, and B. Gault:** Ti and its alloys as examples of cryogenic focused ion beam milling of environmentally-sensitive materials. *Nat. Commun.* **10**, 942 (2019).
53. **K. Hoshino, Y. Iijima, and K.I. Hirano:** Diffusion of vanadium, chromium, and manganese in copper. *Metall. Trans. A* **8**(3), 469 (1977).
54. **B. Sadigh, P. Erhart, A. Stukowski, A. Caro, E. Martinez, and L. Zepeda-Ruiz:** Scalable parallel Monte Carlo algorithm for atomistic simulations of precipitation in alloys. *Phys. Rev. B.* **85**(18), 184203 (2012).

55. **L.A. Giannuzzi and F.A. Stevie:** A review of focused ion beam milling techniques for TEM specimen preparation. *Micron* **30**(3), 197 (1999).
56. **X. Zhou and G.B. Thompson:** The influence of alloying interactions on thin film growth stresses. *Appl. Surf. Sci.* **463**, 545 (2019).
57. **O.C. Hellman, J.A. Vandenbroucke, J. Rüsing, D. Isheim, and D.N. Seidman:** Analysis of three-dimensional atom-probe data by the proximity histogram. *Microsc. Microanal.* **6**(5), 437 (2000).
58. **D.J. Barton, B.C. Hornbuckle, K.A. Darling, and G.B. Thompson:** The influence of isoconcentration surface selection in quantitative outputs from proximity histograms. *Microsc. Microanal.* **25**, 401 (2019).
59. **Y.M. Chen, P.H. Chou, and E.A. Marquis:** Quantitative atom probe tomography characterization of microstructures in a proton irradiated 304 stainless steel. *J. Nucl. Mater.* **451**(1-3), 130 (2014).
60. **L.T. Stephenson, M.P. Moody, P.V. Liddicoat, and S.P. Ringer:** New techniques for the analysis of fine-scaled clustering phenomena within atom probe tomography (APT) data. *Microsc. Microanal.* **13**(6), 448 (2007).
61. **E. Marquis and J. Hyde:** Applications of atom-probe tomography to the characterisation of solute behaviours. *Mater. Sci. Eng., Rep.* **69**(4-5), 37 (2010).
62. **J. Li:** AtomEye: an efficient atomistic configuration viewer. *Modell. Simul. Mater. Sci. Eng.* **11**(2), 173 (2003).
63. **S. Alexander:** Visualization and analysis of atomistic simulation data with OVITO: The Open Visualization Tool. *Modell. Simul. Mater. Sci. Eng.* **18**(1), 015012 (2010).
64. **S. Plimpton:** Fast parallel algorithms for short-range molecular dynamics. *J. Comput. Phys.* **117**, 1 (1995).